Atmos. Meas. Tech. Discuss., 8, 7161–7199, 2015
www.atmos-meas-tech-discuss.net/8/7161/2015/
doi:10.5194/amtd-8-7161-2015

Atmospheric Measurement Techniques Discussions

Radiometric consistency assessment of hyperspectral infrared sounders

L. Wang[1], Y. Han[2], X. Jin[3], Y. Chen[1], and D. A. Tremblay[4]

[1]Earth System Science Interdisciplinary Center/Univ. of Maryland, College Park, MD, USA
[2]NOAA/NESDIS/Center for Satellite Applications and Research, College Park, MD, USA
[3]Earth Resources Technology Inc., Laurel, MD, USA
[4]Science Data Processing Inc., College Park, MD, USA

Received: 15 May 2015 – Accepted: 17 June 2015 – Published: 14 July 2015

Correspondence to: L. Wang (wlikun@umd.edu)

Published by Copernicus Publications on behalf of the European Geosciences Union.

Abstract

The radiometric and spectral consistency among the Atmospheric Infrared Sounder (AIRS), the Infrared Atmospheric Sounding Interferometer (IASI), and the Cross-track Infrared Sounder (CrIS) is fundamental for the creation of long-term infrared (IR) hyperspectral radiance benchmark datasets for both inter-calibration and climate-related studies. In this study, the CrIS radiance measurements on Suomi National Polar-orbiting Partnership (SNPP) satellite are directly compared with IASI on MetOp-A and -B at the finest spectral scale and with AIRS on Aqua in 25 selected spectral regions through one year of simultaneous nadir overpass (SNO) observations to evaluate radiometric consistency of these four hyperspectral IR sounders. The spectra from different sounders are paired together through strict spatial and temporal collocation. The uniform scenes are selected by examining the collocated Visible Infrared Imaging Radiometer Suite (VIIRS) pixels. Their brightness temperature (BT) differences are then calculated by converting the spectra onto common spectral grids. The results indicate that CrIS agrees well with IASI on MetOp-A and IASI on MetOp-B at the longwave IR (LWIR) and middle-wave IR (MWIR) bands with 0.1–0.2 K differences. There are no apparent scene-dependent patterns for BT differences between CrIS and IASI for individual spectral channels. CrIS and AIRS are compared at the 25 spectral regions for both Polar and Tropical SNOs. The combined global SNO datasets indicate that, the CrIS-AIRS BT differences are less than or around 0.1 K among 21 of 25 comparison spectral regions and they range from 0.15 to 0.21 K in the remaining 4 spectral regions. CrIS-AIRS BT differences in some comparison spectral regions show weak scene-dependent features.

1 Introduction

Hyperspectral infrared (IR) radiance measurements from satellite sensors contain valuable information on atmospheric temperature and humidity profiles, greenhouse gases,

AMTD
8, 7161–7199, 2015

clouds, and surface characteristics. These measurements are used not only to retrieve atmospheric temperature and humidity profiles, but more importantly, to be directly assimilated into numerical weather prediction (NWP) models as inputs (Chahine et al., 2006). Moreover, owing to their hyperspectral nature and accurate radiometric and spectral calibration, hyperspectral IR radiances have been used as a reference to independently assess spectral and radiometric calibration accuracy of broad- or narrow-band IR instruments (Goldberg et al., 2011; Wang et al., 2009a, 2011), as well as for long-term climate change monitoring (Wielicki et al., 2013), strict testing of climate model outputs (Huang et al., 2008), and validation of numerical weather model analyses and re-analyses (Wang et al., 2010).

Carried on the NASA's Earth Observing System Aqua spacecraft and launched in May 2002, the Atmospheric Infrared Sounder (AIRS) is a grating infrared sounder that measures the thermal infrared spectrum with 2378 spectral channels covering the 3.74–4.61 μm (2169–2674 cm^{-1}), 6.20–8.22 μm (1217–1614 cm^{-1}), and 8.8–15.4 μm (650–1136 cm^{-1}) spectral bands with a nominal spectral resolution of $\nu/\Delta\nu = 1200$ (Chahine et al., 2006). The Infrared Atmospheric Sounding Interferometer (IASI) is the first operational interferometer in space measuring the 3.5–16.4 μm (610–2825 cm^{-1}) spectrum in 8461 spectral channels with a spectral sampling interval of 0.25 cm^{-1}, successfully launched on MetOp-A in October 2006 and MetOp-B in September 2012 (Hilton et al., 2012). The Cross-track Infrared Sounder (CrIS) on the newly-launched Suomi National Polar-orbiting Partnership (SNPP) and future Joint Polar Satellite System (JPSS) is a Fourier transform spectrometer that provides soundings of the atmosphere with 1305 spectral channels, over 3 wavelength ranges: longwave IR band (LWIR) (9.14–15.38 μm), middle-wave IR band (MWIR) (5.71–8.26 μm), and shortwave IR band (SWIR) (3.92–4.64 μm) (Han et al., 2013). The current SNPP and future JPSS CrIS, combined with the existing AIRS on Aqua and IASI on MetOp-A and -B, will accumulate decades of hyperspectral infrared measurements. Therefore, the radiometric and spectral consistency among AIRS, IASI, and CrIS is fundamental for the creation

AMTD
8, 7161–7199, 2015

of long-term IR hyperspectral radiance benchmark datasets for both inter-calibration and climate-related studies.

In this study, we directly compare the SNPP CrIS radiance measurements with the AIRS on Aqua and IASI on MetOp-A and -B at orbital crossing points of satellites through one year of the data, the so-called simultaneous nadir overpasses (SNO) (Cao et al., 2004). The purpose of this study is to evaluate radiometric consistency and differences of these four hyperspectral IR sounders. This is the first-ever inter-calibration opportunity because four hyperspectral IR sounders observe the Earth and atmosphere at the same spectral regions from different satellites. Several similar studies have been presented recently. For example, D. Jouglet from Centre national d'études spatiales (CNES) (Jouglet et al., 2014) compared IASI (on MetOp-A and -B) with AIRS and CrIS at 33 broad pseudo bands through regional averaging of the soundings pixels over a 300 km × 300 km area around the orbit crossing point with 20 min differences. At each pseudo channel, the inter-compared spectra are averaged to get the similarity of the spectral functions. Tobin et al. (2013a, b) compared CrIS and IASI/MetOp-A along CrIS spectral grids and CrIS with AIRS at 6 spectral ranges with 10 wavenumber intervals, using the so-called "big circle SNOs", where each sounde's observations are averaged within 100 km circle of the SNO location with 20 min time differences. Through collecting a large ensemble of collocated samples, it is believed that the spatial collocation errors are random and Gaussianly distributed. A weighted mean difference between the two sensors is computed independently for each spectral channel by using the spatial variability of each SNO as the weights. Strow et al. (2013a) also compared CrIS with IASI using high-latitude SNO observations and CrIS with AIRS level-1c data that are converted from AIRS level-1b data by removing popping channels and adding the missing channels. All the above studies suggest that the CrIS radiance measurements agree well with these instruments. The uniqueness of this independent study is focused on comparison of four current operational hypepsectral sounders (CrIS with AIRS; CrIS with IASI on MetOp-A and -B) with strict spatial and temporal collocation criteria. We believe that the strict collocation can greatly reduce collocation uncertainties according

AMTD
8, 7161–7199, 2015

to our previous studies and thus can effectively identify the measurement differences at an instrument calibration level if the size of comparison samples is statistically large enough (Wang et al., 2009a, b).

The paper is organized as follows: Sect. 2 briefs CrIS, AIRS, and IASI instruments and the datasets used in this study, Sect. 3 describes the methodology, Sect. 4 presents the results, and Sect. 5 concludes the paper.

2 Instruments and datasets

The instrument characteristics of AIRS, CrIS, and IASI are briefed in Table 1, including satellite platform, launch date, local equator passtime, spatial and spectral resolution, channel number, and spectral coverage. Figure 1 shows typical spectra of AIRS, CrIS, and IASI simulated by the Line-By-Line Radiative Transfer Model (LBLRTM) using a typical tropical atmospheric profile over ocean (Clough et al., 1992, 2005).

AIRS on Aqua is a grating IR spectrometer and disperses the radiation from the Earth scene onto 17 linear arrays of HgCdTe detectors on a focal plane with 2378 IR channels (Chahine et al., 2006). Covering the spectral bands of 3.74–4.61, 6.20–8.22, and 8.8–15.4 µm with a nominal spectral resolution of $\nu/\Delta\nu = 1200$, AIRS views the ground through a cross-track rotary scan mirror and provides ±49.5° ground coverage in every 2.67 s scan cycle. A total of 90 ground footprints are observed for each scan. The AIRS IR spatial resolution is 13.5 km from the nominal altitude of 705.3 km with an ascending node at 13:30 local solar time (LST). The AIRS level 1B Version 5 data are used in this study, which were distributed by NASA Goddard Earth Sciences (GES) Data and Information Services Center (DISC). The overall absolute radiometric calibration accuracy requirement is 3 % in radiance in the infrared spectra (Pagano et al., 2003).

IASI on MetOp-A and -B is a Michelson Interferometer that measures IR radiation emitted from the Earth in the three IR spectral bands between wavelengths of 3.6 and 15.5 µm with a spectral resolution of 0.5 cm^{-1} (after spectral apodization) and a spectral sampling interval of 0.25 cm^{-1} (Hilton et al., 2012). IASI is in a Sun-synchronous

AMTD
8, 7161–7199, 2015

polar orbit at 819 km and crosses the equator at 09:30 LST in a descending node. The IASI observations are obtained by a step scanning mirror covering ±47.85° range in 30 steps in every 8.0 s scan cycle, with 3.3° for each step (normal mode). At each step, the field of regard (FOR) includes 2 × 2 1.25° FOVs (field of view) with a pixel resolution of 12 km at nadir, each positioned in the cross-track and along-track direction located at ±0.825°. We use resampled, apodized, and calibrated spectra with 8461 spectral samples (i.e., the IASI level 1C radiance products), which were directly downloaded from European Organisation for the Exploitation of Meteorological Satellites (EUMETSAT) data center. Hereafter, IASI/A and IASI/B are used to refer to IASI on MetOp-A and MetOp-B in the following parts, respectively.

CrIS is a step-scan Fourier transform spectrometer onboard Suomi NPP spacecraft at a nominal altitude of 824 km in a Sun-synchronous orbit with local equatorial crossing times of ∼ 1:30 p.m. and ∼ 1.30 a.m. CrIS takes 8 s for each scan sweep, each collecting 34 Fields of Regards (FORs). Among them, 30 are the Earth scenes and 4 are the embedded space and blackbody calibration views. The scan mirror stepwise "stares" at the Earth step by step in the cross-track direction from −48.3 to +48.3° with a 3.3° step angle, equaling a 2200 km swath width on the Earth. Nine field stops define the 3 × 3 detector array for each IR wavelength band, which are arrayed as 3 × 3 0.963° circles and separated by 1.1°. The estimated on-orbit absolute spectral calibration uncertainty is less than 3 ppm in the long-wave and midwave bands (Strow et al., 2013b), and the estimated 3 sigma radiometric uncertainty for all Earth scenes is less than 0.3 K in the long-wave band and less than 0.2 K in the midwave and short-wave bands (Tobin et al., 2013b). The geolocation uncertainty for near nadir pixels is less than 0.4 km in the cross-track and in-track directions (Wang et al., 2013). CrIS can be operated in two modes: normal and high spectral resolution mode. CrIS radiance spectrum (without apodization) covers three IR bands from 650 to 1095, 1210 to 1750, and 2155 to 2550 cm^{-1} with spectral resolutions of 0.625, 1.25, and 2.5 cm^{-1} at the normal operational mode (a total of 1305 spectral channels) and with an identical spectral resolution of 0.625 cm^{-1} in all three bands at the full spectral resolution (FSR) mode (a total of

AMTD
8, 7161–7199, 2015

2211 channels). The CrIS instrument is currently operated at normal node, but several tests have been performed at the full spectral resolution mode on 23 February 2012, 12 March and 27 August 2013. CrIS was switched into the FSR mode since 4 December 2014. However, the official CrIS sensor data records (SDR) are still processed and released as the normal resolution by Interface Data Processing Segmen (IDPS).

After launch, an intensive postlaunch evaluation has been performed by the CrIS SDR team, focusing on validating its spectral, radiometric, and geometric calibration. Accordingly, the calibration algorithms have been improved and calibration parameters have been refined during intensive calibration and validation period (Han et al., 2013). The last significant updates took place on 17 February 2014, including (1) the release of IDPS version MX8.2 with correction of central FOV instrument line shape equation and (2) the uploading of Engineering Packets V36 with updated non-linearity coefficients. Therefore, the CrIS radiance data used in this study were processed using JPSS Algorithm Development Library (ADL) version 4.0 with Engineering Packets V36, which is comparable to IDPS version MX8.2. The radiance differences were examined for the data processed by ADL and IDPS and the results suggest that the differences are at the negligible level. As a final note, the CrIS SDR data used in this study has been apodized using a Hamming function (Han et al., 2013).

3 Methods

3.1 Spatial collocation

For pairs of sun-synchronous polar-orbiting satellites with different altitudes, theoretically, their nadir points cross each other within a few seconds near the North and South Polar Regions (typically in the 70–80° N and 70–80° S latitude zones) for a certain time period (dependent on orbit altitude difference), which are referred as SNO observations (Cao et al., 2004). When a SNO occurs, the radiometers from both satellites view the Earth at the same place and same time from different altitudes, which greatly re-

AMTD
8, 7161–7199, 2015

duces the comparison uncertainties related to the difference of satellite observational time and viewing geometries. One of the limitations with high-latitude SNO-based comparison is that the instruments cannot be compared over a wide brightness temperature (BT) dynamic range. However, Aqua and SNPPsatellites basically have the same equatorial crossing time (~ 13:30 LST) but different altitude (SNPP's altitude is 824 km and Aqua's is 705 km). Consequently, every few days, these two satellites are stacked nearly on top of each other with a wealth of coincident data through the full Aqua swath, yielding temporal and spatial coincidences varying with latitude, though with a larger time difference than high-latitude SNOs (Uprety et al., 2013). This provides ample opportunities to compare SNPP CrIS measurements with Aqua AIRS at different latitudes with relatively large dynamic range.

Figure 2a shows time series of SNO latitudes for CrIS-AIRS, CrIS-IASI/A, and CrIS-IASI/B. Since SNPP and Aqua satellites are both in afternoon orbits, the SNO events between SNPP and Aqua occurred every 2 days. They were most concentrated in the South and North Polar Regions and the Tropics, while some were scattered in the mid-latitude regions. On the other hand, since MetOp-A and -B satellites are in mid-morning orbits, the SNOs between MetOp and SNPP occurred every roughly about 50 days. Fortunately, once an SNO event occurs, their orbits cross each other in a number of consecutive orbits when satellites fly to the Polar Regions. Therefore, many SNO observations can be collected during each SNO event. It can be clearly seen in Fig. 2b, showing an enlarged plot of Fig. 2a for a SNO case between CrIS and IASI/B on 1 March 2013.

An example of a SNO event of SNPP and MetOp-A at 18:22 UTC on 27 August 2013 is presented in Fig. 3, where CrIS footprints (indicated by the red circles) and IASI footprints (represented by the blue circles) crossed each other almost at the same time. CrIS (the same as AIRS) has better spatial coverage than IASI. Accordingly, two SNO cases between AIRS on Aqua and CrIS on SNPP are given in Fig. 4, including the Polar SNO case occurring at 21:49 UTC and the Tropical SNO case at 16:15 UTC on 30 August 2013. Different from the CrIS-IASI SNO case, the SNPP and Aqua orbits

AMTD
8, 7161–7199, 2015

follow each other. Therefore, a large of part of their swaths is overlapped. Moreover, CrIS swath is wider than AIRS because the satellite altitude of SNPP is higher than Aqua. Table 2 summarizes the threshold values used for spatial collocation of CrIS and AIRS/IASI FOVs. In order to collocate CrIS FOVs with AIRS and IASI FOVS, we assume that (1) the FOVs of AIRS, CrIS, and IASI are approximately circular at nadir, (2) the spatial response is uniformly distributed within the FOVs, and (3) there is no variation of the spatial response between the different channels (e.g., from longwave channels to shortwave channels). Note that, in reality, the AIRS FOVs were trimmed on both sides by the blinds attached to the AIRS FOV to avoid overlapping effects between neighboring footprints (Schreier et al., 2010).

Considering their different spatial size of FOVs at nadir – 12.0 km for IASI, 13.5 km for AIRS, and 14.0 km for CrIS, we use the distance between two FOVs to pair overlapped FOVs for CrIS and AIRS/IASI. Specifically, a threshold value of 6.0 km is used for CrIS and IASI and 6.875 km is used for CrIS and AIRS. In addition, the observational time and view angle differences (see Table 2 for the specific values) are further examined to filter out the data. Note that the time difference threshold is increased to 15 min for the AIRS-CrIS Tropical SNOs because of their large time differences (Uprety et al., 2013).

Finally, for a typical interferometer like CrIS or IASI, instrument FOV geometry (including beam divergence introduced by finite FOV and off-axis effects cause by its position on a focal plane) and instrument imperfections (such as various optical, mechanical, and electrical imperfections of the interferometer system during the sweep of the optical path difference) impose an apodization function on its interferogram or the so-called self-apodization. The self apodizatio of the interferogram results in an instrument line shape (ILS) that is shifted and stretched in frequency a well as an amplitude reduction, which has been well corrected for CrIS and IASI spectra. However, radiance nonuniformity within the instrumen's FOV also affects ILS associated with each true wavenumber, which has not been taken into account in CrIS and IASI radiance product (Genest and Tremblay, 1999; Tobin et al., 2009). Moreover, inhomogeneous scenes can introduce spatial collocation uncertainties owing to the different point spread func-

AMTD
8, 7161–7199, 2015

tions of CrIS and IASI/AIRS. To avoid these uncertainties, only uniform FOVs are selected. We use the collocated Visible Infrared Imaging Radiometer Suite (VIIRS) pixels to check CrIS FOV homogeneity by examining the standard deviation to the mean ratio of the VIIRS band M16 (with central wavelength of 11.8 µm) radiances from the pixels falling in corresponding CrIS FOVs (Wang et al., 2013). Onboard the same satellite platform, VIIRS is a whiskbroom scanning imaging radiometer, collecting visible and infrared imagery of the Earth through 22 spectral bands between 0.412 and 12.01 µm. These bands include 16 moderate resolution bands (M-bands) with a spatial resolution of 750 m at nadir, 5 imaging resolution bands (I-bands) with a 375 m at spatial resolution nadir, and 1 panchromatic day-night band (DNB) with a 750 m spatial resolution throughout the scan. VIIRS has four bands that are fully overlapped with CrIS, that is M13 (4.07 µm), M15 (10.7 µm), M16 (11.8 µm) and I5 (11.45 µm). Intercomparison between CrIS and VIIRS indicate good agreement between M16 and CrIS (Wang et al., 2012) and therefore VIIRS M16 band is used to characterize the CrIS scene uniformity. Demonstrated in Fig. 5 is the BT difference between CrIS and IASI/B at 900 cm^{-1} vs. the standard deviation to mean ratio of the VIIRS radiances in band M16. It shows that, with a larger ratio, the spread of the BT difference becomes larger, whereas the BT differences converge when the ratio values decrease. From a practical point of view, this ratio is an effective method to constrain scene homogeneity to reduce the comparison uncertainties, specifically when a smaller value is chosen.

Figure 6 gives the mean spectra of paired CrIS and IASI SNO FOVs for the SNO event shown in Fig. 3. During this SNO event, the full resolution mode was operated for SNPP CrIS. Accordingly, CrIS spectra are collocated at the full resolution mode, indicated by red lines (Chen et al., 2014). The full resolution spectra can be further processed to be the normal mode data (like current officially-released CrIS SDR data) by the ADL software, which are represented by blue lines in Fig. 6. In order to clearly show the agreement between CrIS and IASI, an enlarged plot is given in Fig. 6b at the spectral range from 2200–2400 cm^{-1}. Overall, it clearly shows that the CrIS and IASI absorption spectral lines well matched. However, in order to quantify the detailed

AMTD
8, 7161–7199, 2015

differences between them, we need to convert CrIS and IASI onto common spectral grids, which are discussed below.

3.2 Spectral match

This part describes the method of how to convert paired CrIS-IASI and CrIS-AIRS spectra onto common spectral grids in order to quantify their radiometric differences.

3.2.1 CrIS vs. IASI

Both CrIS and IASI are Fourier Transform Infrared (FT-IR) spectrometers. Given that IASI has a longer optical path difference (OPD) (2.0 cm for all three bands) than CrIS (0.8 cm for LWIR band, 0.4 for MWIR band, and 0.2 for SWIR band), IASI has higher spectral resolution than CrIS (see Table 1). Thus, it is straightforward to convert IASI spectra into CrIS spectral grids. Specifically, five steps are performed, including: (1) converting IASI spectra to interferograms using Fourier transform; (2) de-apodizing IASI interferograms using IASI apodization functions; (3) truncating the IASI interferograms based on CrIS OPD specification, (4) apodizing truncated interferograms using CrIS Hanning apodization functions; and (5) transforming interferograms back into spectra using inverse Fourier transform.

Shown in Fig. 7a are CrIS and IASI spectra simulated by LBLRTM using an identical atmospheric profile as inputs. Theoretically, these two spectra should be consistent to each other with negligible differences. Figure 7b gives their spectral differences by using the above steps to convert IASI spectra onto CrIS spectral grids. The results suggest that the method is very accurate and re-sampling errors are less than 0.02 K for all three bands.

3.2.2 CrIS vs. AIRS

For AIRS and CrIS, it is a challenging task to covert AIRS and CrIS onto a common spectral domain. As a grating spectrometer, AIRS spectral resolution varies with dif-

AMTD
8, 7161–7199, 2015

ferent bands, and spectral gaps exist due to the design (see Fig. 1). Moreover, the observations from some channels are not in good quality due to the bad or degraded detectors (the channel property list can be found at http://disc.sci.gsfc.nasa.gov/AIRS/documentation/v5_docs). To date, 274 of 2378 AIRS channels are not recommended for use. Due to the above consideration, the inter-comparison between CrIS and AIRS are focused on 25 spectral regions, as shown in the grey bars in Fig. 8 (the spectral range can be found in Table 3). Specifically, the radiance values falling within the each comparison region are averaged together, respectively for CrIS and AIRS spectra. The radiances for AIRS bad channels are linearly interpolated using the values from neighboring channels. The averaged radiance values are then converted into brightness temperature through the mean wavenumber. While this match method cannot compare AIRS and CrIS at the finest spectral scale like CrIS and IASI, we do believe that this method can minimize the issues due to the difference of AIRS and CrIS instrument design and spectral response, and thus can produce more meaningful assessment of the radiometric differences between CrIS and AIRS. The similar band-average methods are also utilized by Jouglet et al. (2014) who selected 33 spectral regions to compare CrIS with IASI as well as by Tobin et al. (2013b) who selected 6 spectral regions with 10 wavenumber interval to compare CrIS with AIRS. As shown in Fig. 8, for the LBLRTM-simulated simulated AIRS and CrIS spectra using an identical atmospheric profile, the BT differences using above average method can be reduced to less than 0.06 K with consideration of AIRS degraded channels.

3.3 Data processing

After the above two steps, the CrIS-AIRS and CrIS-IASI spectra are spatially and spectrally matched together. A whole year of data in 2013 is processed based on the above steps, including CrIS-IASI/A, CrIS-IASI/B, and CrIS-AIRS. For each pair of sensors, the SNO observations are categorized into the SNO observations at the North Polar Region (North SNOs), those at the South Polar Region (South SNOs), and those in the

AMTD
8, 7161–7199, 2015

Tropics (Tropical SNOs, CrIS-AIRS only). Specially, for CrIS-AIRS SNO data, since the SNO event happed every two days, the data are further averaged on a daily basis.

4 Results and discussion

4.1 CrIS vs. IASI

Based on the collocation criteria, a total of 2748 pairs of spectra are collocated for CrIS and IASI-A in 2013, which is composed by 1274 pairs from North SNOs and and 1474 pairs from South SNOs. For CrIS and IASI-B, there are a total of 2008 pairs of the SNO spectra in 2013, categorized as 952 pairs from North SNOs and 1056 pairs from South SNOs, which are less than CrIS-IASI/A due to the fact that IASI-B data were distributed under operational mode since 24 April 2013.

Figures 9a and 10a show CrIS spectral distribution for CrIS-IASI/A and CrIS-IASI/B SNO observations, where the red lines indicate the observations for North SNOs and the blue lines represents those for South SNOs. If one examines the spectra at the atmospheric window regions (850–900 cm^{-1}), the BT values range from 220 to 290 K in North SNOs while they range from 190 to 270 K in South SNOs. This suggests that CrIS-IASI SNO observations have a relatively large dynamic range for both CrIS-IASI/A and CrIS-IASI/B SNO samples. The mean and standard deviation of BT differences of CrIS-IASI/A are given in Fig. 9b, while those from CrIS-IASI/B are shown in Fig. 10b. At LWIR and MWIR bands, CrIS agrees well with IASI and the BT differences are less than 0.2 K, while the standard deviation ranges from 0.2 to 0.7 K dependent on different spectral absorption regions. Compared with both IASI/A and IASI/B, CrIS is slightly warmer than IASI (less than 0.2 K) at most spectral regions. These results are encouraging because the spectra at these two bands are mainly used as inputs for NWP data assimilation and retrieval of atmospheric temperature and humidity profiles. However, at SWIR band, the BT differences range from 0.2 to 1.0 K and the standard deviation also increases, especially for the South SNOs. The explanation of the large

AMTD
8, 7161–7199, 2015

standard deviation probably is due to the large noise equivalent differential temperature (NEDT) at the shortwave band for cold scenes for both CrIS and IASI. When one examines the mean BT differences of CrIS-IASI, a considerable sharp increase can be found at spectral line transition region (around 2400 cm^{-1}), which are shown in both Figs. 9b and 10b. It is probably caused by two reasons. First, given a relatively large spectral resolution of 2.5 cm^{-1} for the SWIR band, it is challenging to achieve the same spectral accuracy as the LWIR and SWIR bands (Strow et al., 2013b). Therefore, the spectral calibration for SWIR band is not as good as LWIR and MWIR bands. Secondly, it is speculated that there is small non-linear response for the detectors in SWIR band, which currently are treated as linear detectors and there is no non-linear correction for CrIS SWIR band (D. Tobin, personal communication, 2014). However, the investigations are not conclusive at this point and the root cause is still under investigation.

When one carefully compares CrIS-IASI/A and CrIS-IASI/B results, especially for results of the South SNO samples, we can find that CrIS-IASI/A and CrIS-IASI/B are slightly different. If one treats CrIS as a transfer radiometer and then CrIS measurements are assumed to be canceled out, the double differences of CrIS-IASI/B and CrIS-IASI/A indicate that IASI/B is slightly warmer (less than 0.1 K) than IASI/A in LWIR bands and they are consistent to each other well in MWIR bands. The observed differences between IASI-A and IASI-B in the longwave band are suspected to be due to imperfections in the respective nonlinearity corrections. This result agrees well with the findings by D. Jouglet from CNES (Jouglet et al., 2014), who directly compared IASI/A and IASI/B spectra with 50 min difference.

In order to show how the BT differences are dependent on scene temperatures, scatter plots of CrIS-IASI BT differences vs. CrIS BTs at three individual channels (including one CO_2 absorption channel, one longwave window channel, and one water vapor channel) shown in Fig. 11 for CrIS-IASI/A and in Fig. 12 for CrIS-IASI/B, correspondingly. Specifically, the red dots indicate the observations from North SNOs and the blue dots represent those from South SNOs, while the green lines give the linear fitting line. For all three individual channels, the slope of linear regression is very small,

AMTD
8, 7161–7199, 2015

indicating that there is no strong scene dependent features. This also implies for the BT differences between CrIS and IASI/B, shown in Fig. 12. However, it is necessary to point out that CrIS-IASI comparison is only limited to relatively cold scenes in the Polar Regions and the comprehensive assessment of CrIS-IASI radiometric consistency still needs to be extended to the low latitude regions in the future.

4.2 CrIS vs. AIRS

The CrIS-AIRS SNO comparison results are shown in Fig. 13, including CrIS spectral distribution and the mean and standard deviation of CrIS-AIRS BT difference. They are categorized into North, South, and Tropical SNOs and the global dataset that combines all three SNO datasets together. In addition, the statistics of CrIS-AIRS BT differences along the 25 spectral regions are summarized in Table 3. The SNO spectral distribution clearly shows the characteristic in different climate regions if one visually inspects the dynamic range of the BT values at the atmospheric window region. In other words, the BTs from Tropical SNOs (ranging from 265 to 310 K) are different from Polar SNOs (ranging from 210 to 280 K). The following findings are revealed based on Fig. 13 and Table 3. First, at the 650–681.875 and 690–710 cm^{-1} spectral regions in LWIR band, CrIS is warmer than AIRS for all three SNO datasets and the BT differences range from 0.026 to 0.167 K. At the other 10 spectral regions (spectral region 3–11 and 12 in Table 3) in LWIR band, CrIS and AIRS agree well and the BT differences are less than 0.1 K for North and South SNOs; however, CrIS is warmer than AIRS by $\sim$ 0.1 K for Tropical SNOs. At the ozone absorption region of 1075–1095 cm^{-1} in LWIR band, CrIS is slightly colder than AIRS and the BT differences range from −0.02 to −0.161 K. Second, among 6 of 8 spectral regions (spectral region 14–19 in Table 3) in the MWIR band, CrIS-AIRS BT differences are less than or around 0.1 K for all three SNO datasets. Only at the 1240.50–1262.00 and 1591.25–1613.00 cm^{-1} spectral regions, BT differences are larger than 0.15 K in some SNO datasets. Finally, in the SWIR band, CrIS is warmer than AIRS from 0.01–0.42 K for South and North SNOs but their agreement is much better for Tropical SNOs. To combine the three

AMTD
8, 7161–7199, 2015

SNO datasets together, Fig. 13 and Table 3 also summarize the global CrIS-AIRS BT difference statistics. Generally speaking, among 21 of 25 comparison spectral regions, the CrIS-AIRS BT differences are less than or around 0.1 K; in the remaining 4 spectral regions (one in the LWIR band and three in the SWIR band), the BT differences range from 0.15 to 0.21 K. Moreover, among 16 of 25 spectral regions, CrIS is slightly warmer than AIRS.

Given the fact that each SNO dataset has its own unique BT distribution, it is possible to check their BT differences vs. scene BTs with a relatively large dynamic range. Four spectral regions are selected, including the CO_2 absorption region (650–681.88 cm^{-1}), the atmospheric window region (889–903 cm^{-1}), the water vapor absorption region (1380–1410 cm^{-1}), and the shortwave region (2190–2260 cm^{-1}). Combining three SNO dataset together, Fig. 14 gives CrIS-AIRS BT differences varying with CrIS BTs, where the red, blue, and black dots indicate the data from North, South, and Tropical SNOs, respectively. Specifically, the BT differences at the CO_2 absorption and shortwave regions show weak scene-dependent features. At the atmospheric window region, there is no scene-dependent feature for Polar SNOs (range from 210 to 270 K), but the BT difference increase with the scene BTs for Tropical SNOs when BTs are larger than 270 K. Finally, at the water vapor absorption region, there is no scene-dependent feature. One explanation of these scene-dependent features can be due to the imperfection of instrument's non-linearity correction. For AIRS and CrIS instrument, non-linearity correction has been performed during radiometric calibration to correct the non-linear response for the instrument detectors (Pagano et al., 2003; Tobin et al., 2013b). The deficiency of non-linearity correction for one or both of instruments can result in this kind of scene-dependent patterns based on the previous study (Tobin et al., 2013b). Figure 15 shows the AIRS-CrIS BT difference time series at the four spectral regions. The BT difference time series at the CO_2 absorption and shortwave regions for polar SNOs show weak seasonal variations, which can be well explained by the scene-dependent BT difference features shown in Fig. 14. In other time series of the BT differences, there are no apparent seasonal variation and long term trend.

AMTD
8, 7161–7199, 2015

5 Conclusions

The radiometric and spectral consistency among AIRS, IASI, and CrIS is fundamental for the creation of long-term IR hyperspectral radiance benchmark dataset for both inter-calibration and climate-related studies. In this study, we directly compare the SNPP CrIS radiance measurements with IASI on MetOp-A and -B at the finest spectral scale and with AIRS on Aqua at selected 25 spectral regions through one year's SNO observations to evaluate radiometric consistency and differences of these four hyperspectral IR sounders. The spectra from different sounders are paired together through strict spatial and temporal collocation. The uniform scenes are selected by examining the collocated VIIRS pixels. The radiometric BT differences are then calculated by converting the spectra onto common spectral grids. The following conclusion can be drawn based on our analysis.

1. CrIS agrees well with IASI on MetOp-A and IASI on MetOp-B at LWIR and MWIR bands with 0.1–0.2 K differences and CrIS is slightly warmer than IASI.
2. The large BT differences are found at the spectral transition region (about 2400 cm^{-1}) at SWIR band for both CrIS-IASI/A and CrIS-IASI/B SNO datasets. The root cause still needs further investigation in the future.
3. CrIS-IASI BT differences show weak scene-dependent patterns revealed from both CrIS-IASI/A and CrIS-IASI/B SNO datasets, which, however, are limited to the observations at the Polar Regions.
4. CrIS and AIRS are compared along the 25 spectral regions for both Polar and Tropical SNOs. The combined global SNO datasets indicate that, the CrIS-AIRS BT differences are less than or around 0.1 K among 21 of 25 comparison spectral regions and they range from 0.15 to 0.21 K in the remaining 4 spectral regions. Moreover, among 16 of 25 spectral regions, CrIS is slightly warmer than AIRS. CrIS-AIRS BT differences shows weak scene-dependent features in some comparison spectral regions.

AMTD
8, 7161–7199, 2015

As a final note, we point out that, due to the huge volume of AIRS, IASI, and CrIS data, this study is only limited to one year's period. CrIS has been operated in the full spectral resolution mode with 2211 channels since December 2014. This comparison will be extended to CrIS full resolution spectra to further examine the consistence of CrIS with AIRS and IASI.

Acknowledgements. The VIIRS and IASI data for this paper are available at NOAA's Comprehensive Large Array Data Stewardship System. The AIRS data are available at NASA Goddard Earth Sciences (GES) Data and Information Services Center (DISC). The IASI data can also be downloaded from European Organisation for the Exploitation of Meteorological Satellites (EUMETSAT) data center. The CrIS data for this paper are available at the data server at NOAA/NESDIS/STAR and can be obtained by contacting the authors at wlikun@umd.edu. The authors thank the anonymous reviewers, Fangfang Yu, and Frank Padula for providing valuable comments for the study. This study is funded by the NOAA JPSS Program Office. Likun Wang and Yong Chen are also supported by NOAA grant NA14NES4320003 (Cooperative Institute for Climate and Satellites) at the University of Maryland/ESSIC. The manuscript contents are solely the opinions of the authors and do not constitute a statement of policy, decision, or position on behalf of NOAA or the US government.

References

Cao, C., Weinreb, M., and Xu, H.: Predicting simultaneous nadir overpasses among polar-orbiting meteorological satellites for the intersatellite calibration of radiometers, J. Atmos. Ocean. Tech., 21, 537–542, 2004.

Chahine, M. T., Pagano, T. S., Aumann, H. H., Atlas, R., Barnet, C., Blaisdell, J., Chen, L., Divakarla, M., Fetzer, E. J., Goldberg, M., Gautier, C., Granger, S., Hannon, S., Irion, F. W., Kakar, R., Kalnay, E., Lambrigtsen, B. H., Lee, S.-Y., Le Marshall, J., Wallace McMillan, W., McMillin, L., Olsen, E. T., Revercomb, H., Rosenkranz, P., Smith, W. L., Staelin, D., Strow, L. L., Susskind, J., Tobin, D., Wolf, W. and Zhou, L. : AIRS: improving weather forecasting and providing new data on greenhouse gases, B. Am. Meteorol. Soc., 87, 911–926, 2006.

AMTD
8, 7161–7199, 2015

Chen, Y., Han, Y., Tremblay, D., Wang, L., Jin, X., and Weng, F.: Assessment of S-NPP CrIS full resolution SDR radiometirc and spectral accuracy, in: The 94th American Meteorological Society Annual Meeting, 2–6 February 2014, 9.4, Atlanta, Georgia, 2014.

Clough, S. A., Iacono, M. J., and Moncet, J.-L.: Line-by-line calculations of atmospheric fluxes and cooling rates: application to water vapor, J. Geophys. Res.-Atmos., 97, 15761–15785, doi:10.1029/92jd01419, 1992.

Clough, S. A., Shephard, M. W., Mlawer, E. J., Delamere, J. S., Iacono, M. J., Cady-Pereira, K., Boukabara, S., and Brown, P. D.: Atmospheric radiative transfer modeling: a summary of the AER codes, J. Quant. Spectrosc. Ra., 91, 233–244, doi:10.1016/j.jqsrt.2004.05.058, 2005.

Genest, J. and Tremblay, P.: Instrument line shape of Fourier transform spectrometers: analytic solutions for nonuniformly illuminated off-axis detectors, Appl. Optics, 38, 5438–5446, doi:10.1364/ao.38.005438, 1999.

Goldberg, M., Ohring, G., Butler, J., Cao, C., Datla, R., Doelling, D., Gärtner, V., Hewison, T., Iacovazzi, B., Kim, D., Kurino, T., Lafeuille, J., Minnis, P., Renaut, D., Schmetz, J., Tobin, D., Wang, L., Weng, F., Wu, X., Yu, F., Zhang, P., and Zhu, T.: The global space-based iinter-calibration system, B. Am. Meteorol. Soc., 92, 467–475, doi:10.1175/2010bams2967.1, 2011.

Han, Y., Revercomb, H., Cromp, M., Gu, D., Johnson, D., Mooney, D., Scott, D., Strow, L., Bingham, G., Borg, L., Chen, Y., DeSlover, D., Esplin, M., Hagan, D., Jin, X., Knuteson, R., Motteler, H., Predina, J., Suwinski, L., Taylor, J., Tobin, D., Tremblay, D., Wang, C., Wang, L., Wang, L., and Zavyalov, V.: Suomi NPP CrIS measurements, sensor data record algorithm, calibration and validation activities, and record data quality, J. Geophys. Res.-Atmos., 118, 2013JD020344, doi:10.1002/2013jd020344, 2013.

Hilton, F., Armante, R., August, T., Barnet, C., Bouchard, A., Camy-Peyret, C., Capelle, V., Clarisse, L., Clerbaux, C., Coheur, P.-F., Collard, A., Crevoisier, C., Dufour, G., Edwards, D., Faijan, F., Fourrié, N., Gambacorta, A., Goldberg, M., Guidard, V., Hurtmans, D., Illingworth, S., Jacquinet-Husson, N., Kerzenmacher, T., Klaes, D., Lavanant, L., Masiello, G., Matricardi, M., McNally, A., Newman, S., Pavelin, E., Payan, S., Péquignot, E., Peyridieu, S., Phulpin, T., Remedios, J., Schlüssel, P., Serio, C., Strow, L., Stubenrauch, C., Taylor, J., Tobin, D., Wolf, W., and Zhou, D.: Hyperspectral Earth observation from IASI: five years of accomplishments, B. Am. Meteorol. Soc., 93, 347–370, doi:10.1175/bams-d-11-00027.1, 2012.

Huang, X., Yang, W., Loeb, N. G., and Ramaswamy, V.: Spectrally resolved fluxes derived from collocated AIRS and CERES measurements and their application in model

AMTD
8, 7161–7199, 2015

evaluation: clear sky over the tropical oceans, J. Geophys. Res.-Atmos., 113, D09110, doi:10.1029/2007jd009219, 2008.
Jouglet, D., Chinaud, J., and Lenot, X.: Radiometric inter-comparison of IASI:IASI-A/IASI-B, IASI/AIRS, IASI/CrIS, in: The 2014 EUMETSAT Meteorological Satellite Conference, 22–26 September 2014, 205, Geneva, Switzerland, 2014.
Pagano, T. S., Aumann, H. H., Hagan, D. E., and Overoye, K.: Prelaunch and in-flight radiometric calibration of the Atmospheric Infrared Sounder (AIRS), IEEE T. Geosci. Remote, 41, 265–273, doi:10.1109/tgrs.2002.808324, 2003.
Schreier, M. M., Kahn, B. H., Eldering, A., Elliott, D. A., Fishbein, E., Irion, F. W., and Pagano, T. S.: Radiance comparisons of MODIS and AIRS using spatial response information, J. Atmos. Ocean. Tech., 27, 1331–1342, doi:10.1175/2010jtecha1424.1, 2010.
Strow, L., Motteler, H., Schou, P., and Hannon, S. E.: Intercalibration of IASI with AIRS and CrIS the Third Infrared Atmospheric Sounding Interferometer conference, 4–8 February 2013, Hyères, France, 2013a.
Strow, L. L., Motteler, H., Tobin, D., Revercomb, H., Hannon, S., Buijs, H., Predina, J., Suwinski, L., and Glumb, R.: Spectral calibration and validation of the Cross-track Infrared Sounder on the Suomi NPP satellite, J. Geophys. Res.-Atmos., 118, 12486–412496, doi:10.1002/2013jd020480, 2013b.
Tobin, D., Revercomb, H., and Antonelli, P.: Principal Component Analysis of IASI Spectra with a Focus on Non-Uniform Scene Effects on the ILS, Current Problems in Atmospheric Radiation (IRS 2008): Proceedings of the International Radiation Symposium (IRC/IAMAS), 3–8 August 2008, Foz do Iguaçu , Brazil, AIP Publishing, 16–19, 2009.
Tobin, D., Revercomb, H., Knuteson, B., Best, F., Taylor, J., Deslover, D., Borg, L., Moeller, C., Martin, G., Kuehn, R., Quinn, G., and Garcia, R.: Soumi NPP/JPSS Cross-Track Infrared Sounder (CrIS): Intercalibration with AIRS, IASI, and VIIRS, in: The 93rd AMS Annual Meeting, 6–10 January 2013, P700, Austin, Texas, 2013a.
Tobin D., Revercomb, H., Knuteson, R., Taylor, J., Best, F., Borg, L., DeSlover, D., Martin, G., Buijs, H., Esplin, M., Glumb, R., Han, Y., Mooney, D., Predina, J., Strow, L., Suwinski, L., and Wang, L.: Suomi-NPP CrIS radiometric calibration uncertainty, J. Geophys. Res.-Atmos., 118, 10589–510600, doi:10.1002/jgrd.50809, 2013b.
Uprety, S., Cao, C., Xiong, X., Blonski, S., Wu, A., and Shao, X.: Radiometric intercomparison between Suomi-NPP VIIRS and aqua MODIS reflective Solar bands using si-

AMTD
8, 7161–7199, 2015

multaneous nadir overpass in the low latitudes, J. Atmos. Ocean. Tech., 30, 2720–2736, doi:10.1175/jtech-d-13-00071.1, 2013.
Wang, L., Cao, C., and Goldberg, M.: Intercalibration of GOES-11 and GOES-12 water vapor channels with MetOp IASI Hyperspectral Measurements, J. Atmos. Ocean. Tech., 26, 1843–1855, doi:10.1175/2009jtecha1233.1, 2009a.
Wang, L., Wu, X., Goldberg, M., Cao, C., Li, Y., and Sohn, S.-H.: Comparison of AIRS and IASI radiances using GOES imagers as transfer radiometers toward climate data records, J. Appl. Meteorol. Clim., 49, 478–492, doi:10.1175/2009jamc2218.1, 2009b.
Wang, L., Goldberg, M., Liu, X., and Zhou, L.: Assessment of reanalysis datasets using AIRS and IASI hyperspectral radiances, Geoscience and Remote Sensing Symposium (IGARSS), 2010 IEEE International, Honolulu, Hawaii, USA, 25–30 July 2010, 2936–2939, 2010.
Wang, L., Goldberg, M., Wu, X., Cao, C., Iacovazzi Jr., R. A., Yu, F., and Li, Y.: Consistency assessment of atmospheric infrared sounder and infrared atmospheric sounding interferometer radiances: double differences versus simultaneous nadir overpasses, J. Geophys. Res., 116, D11111, doi:10.1029/2010jd014988, 2011.
Wang, L., Han, Y., Tremblay, D., Weng, F., and Goldberg, M.: Inter-comparison of NPP/CrIS radiances with VIIRS, AIRS, and IASI: a post-launch calibration assessment, Proc. SPIE 8528, , Earth Observing Missions and Sensors: Development, Implementation, and Characterization II, 85280J, doi:10.1117/12.978769, 2012.
Wang, L., Tremblay, D. A., Han, Y., Esplin, M., Hagan, D. E., Predina, J., Suwinski, L., Jin, X., and Chen, Y.: Geolocation assessment for CrIS sensor data records, J. Geophys. Res.-Atmos., 118, 12690–612704, doi:10.1002/2013jd020376, 2013.
Wielicki, B. A., Young, D. F., Mlynczak, M. G., Thome, K. J., Leroy, S., Corliss, J., Anderson, J. G., Ao, C. O., Bantges, R., Best, F., Bowman, K., Brindley, H., Butler, J. J., Collins, W., Dykema, J. A., Doelling, D. R., Feldman, D. R., Fox, N., Huang, X., Holz, R., Huang, Y., Jin, Z., Jennings, D., Johnson, D. G., Jucks, K., Kato, S., Kirk-Davidoff, D. B., Knuteson, R., Kopp, G., Kratz, D. P., Liu, X., Lukashin, C., Mannucci, A. J., Phojanamongkolkij, N., Pilewskie, P., Ramaswamy, V., Revercomb, H., Rice, J., Roberts, Y., Roithmayr, C. M., Rose, F., Sandford, S., Shirley, E. L., Smith, W. L., Soden, B., Speth, P. W., Sun, W., Taylor, P. C., Tobin, D., and Xiong, X.: Achieving climate change absolute accuracy in orbit, B. Am. Meteorol. Soc., 94, 1519–1539, doi:10.1175/bams-d-12-00149.1, 2013.

AMTD
8, 7161–7199, 2015

Table 1. Instrument characteristics of CrIS, AIRS, and IASI.

	CrIS	AIRS	IASI
Satellite Platform	Suomi NPP	Aqua	MetOp-A MetOp-B
Launch Date	28 Oct 2011	4 May 2002	19 Oct 2006 17 Sep 2012
Local equatorial crossing times	13:30	13:30	09:30
Spatial Resolution (nadir)	14.0 km	13.5 km	12 km
Technique	FTS[a]	Grating	FTS
Number of Channels	1305 (Normal spectral resolution) 2211 (Full spectral resolution)	2378	8461
Spectral Coverage	LWIR, MWIR and SWIR with gaps	17 spectral bands with gaps	LWIR, MWIR, SWIR bands without gaps
Spectral sampling resolution (cm^{-1})	LWIR: 0.625 (0.625)[b] MWIR: 1.25 (0.625) SWIR: 2.5 (0.625)	0.4–2.1 (varying with bands)	0.25
Reference	Han et al. (2013)	Chahine et al. (2006)	Hilton et al. (2011)

[a] FTS represents Fourier Transform Sounder.

[b] The numbers in the brackets indicate the spectral resolution at full spectral resolution mode.

AMTD
8, 7161–7199, 2015

Table 2. Collocation criterion for CrIS-AIRS and CrIS-IASI SNOs.

Condition	Criterion
FOV distance	CrIS and IASI: ≤ 6.0 km CrIS and AIRS: ≤ 6.875 km
Time Difference	≤ 2 min for high latitude SNOs ≤ 15 min for low latitude SNOs between CrIS and AIRS
View Angle Differences	abs(cos(zen1)–cos(zen2)) ≤ 0.01*
FOV homogeneity	STDDEV(VIIRS_M16)/MEAN(VIIRS_M16) < 5 %

* zen1 and zen2 are the zenith angles of paired FOVs from two instruments.

AMTD
8, 7161–7199, 2015

Table 3. Statistics of CrIS-AIRS BT Differences at 25 Spectral Regions.

	Spectral Range	North SNOs		South SNOs		Tropical SNOs		Global	
	(cm^{-1})	Mean (K)	SD (K)	Mean (K)	SD (K)	Mean (K)	SD (K)	Mean (K)	SD (K)
1	650.000–681.875	0.1025	0.0432	0.0538	0.0300	0.0261	0.0265	0.0500	0.0443
2	690.000–710.000	0.1661	0.0642	0.1201	0.0751	0.1572	0.0227	0.1509	0.0528
3	733.500–755.000	−0.0297	0.1292	−0.0348	0.0921	0.1088	0.0854	0.0444	0.1210
4	760.000–781.750	−0.0215	0.1674	−0.0045	0.0980	0.1180	0.1292	0.0581	0.1482
5	800.000–830.000	0.0006	0.1725	0.0192	0.1044	0.1688	0.1452	0.0962	0.1645
6	830.000–849.000	−0.0526	0.1781	−0.0384	0.1116	0.1072	0.1502	0.0374	0.1678
7	860.000–887.000	−0.0318	0.1822	−0.0244	0.1106	0.0910	0.1470	0.0366	0.1601
8	889.000–903.000	−0.0209	0.1803	−0.0104	0.1138	0.1382	0.1536	0.0679	0.1705
9	911.250–941.250	−0.0304	0.1849	−0.0247	0.1125	0.1280	0.1509	0.0570	0.1705
10	941.250–973.750	0.0136	0.1859	0.0241	0.1172	0.1265	0.1470	0.0773	0.1601
11	977.375–1010.00	−0.0008	0.1856	0.0794	0.1212	0.0124	0.1396	0.0245	0.1506
12	1075.00–1095.00	−0.1614	0.2092	−0.1455	0.1725	−0.0210	0.1474	−0.0816	0.1815
13	1240.50–1262.00	0.0477	0.1456	0.0543	0.0816	0.1694	0.0995	0.1153	0.1234
14	1285.00–1338.75	−0.0145	0.1069	0.0285	0.0697	0.0237	0.0709	0.0160	0.0820
15	1355.00–1381.00	−0.0679	0.0968	−0.0246	0.0806	−0.0505	0.0752	−0.0486	0.0830
16	1380.00–1410.00	0.0031	0.0945	0.0265	0.0804	0.0155	0.0800	0.0151	0.0839
17	1415.00–1435.00	−0.0127	0.0736	−0.0112	0.0617	0.0368	0.0843	0.0145	0.0809
18	1461.25–1495.00	−0.0701	0.0669	−0.0281	0.0571	−0.0846	0.0863	−0.0685	0.0795
19	1561.25–1591.25	−0.0857	0.0697	−0.0953	0.0418	−0.0438	0.0883	−0.0651	0.0793
20	1591.25–1613.00	−0.1649	0.1512	−0.1710	0.1545	−0.0459	0.0939	−0.1017	0.1383
21	2190.00–2260.00	0.2110	0.0851	0.2536	0.0758	0.1930	0.0713	0.2109	0.0794
22	2260.00–2285.00	0.3165	0.1506	0.4216	0.2986	0.0341	0.0713	0.1869	0.2390
23	2310.00–2340.00	0.1168	0.2300	0.0113	0.1591	−0.1134	0.0459	−0.0321	0.1677
24	2360.00–2400.00	0.1827	0.1009	0.2061	0.1010	0.1195	0.0622	0.1537	0.0905
25	2447.50–2475.00	0.0110	0.1810	0.0757	0.3196	0.0240	0.2170	0.0327	0.2380

AMTD
8, 7161–7199, 2015

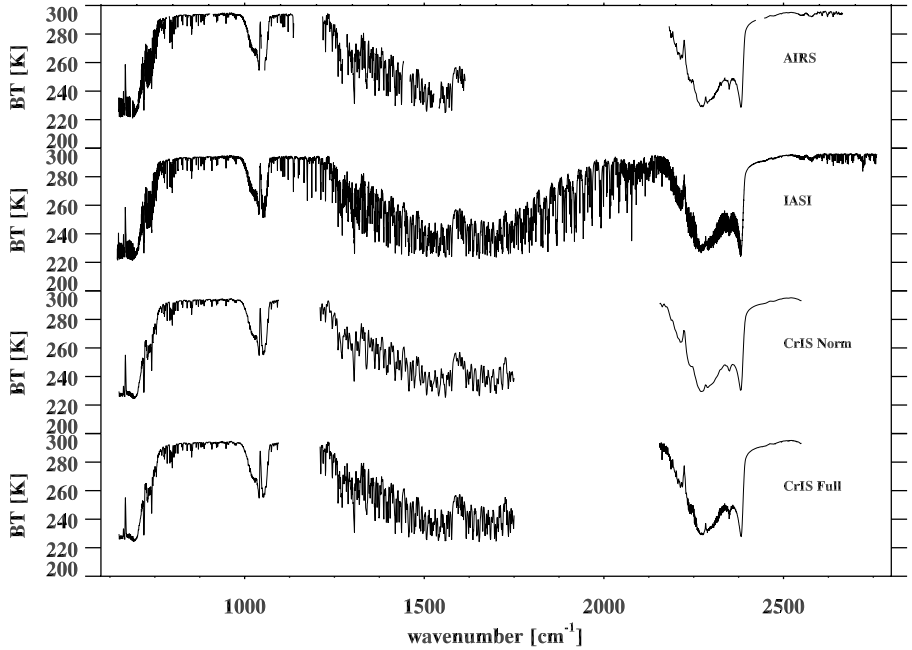

Figure 1. AIRS, CrIS, and IASI Spectra simulated by LBLRTM using an identical tropical atmospheric profile over ocean. The description of CrIS normal and full spectral resolution mode can be found in the text part.

AMTD
8, 7161–7199, 2015

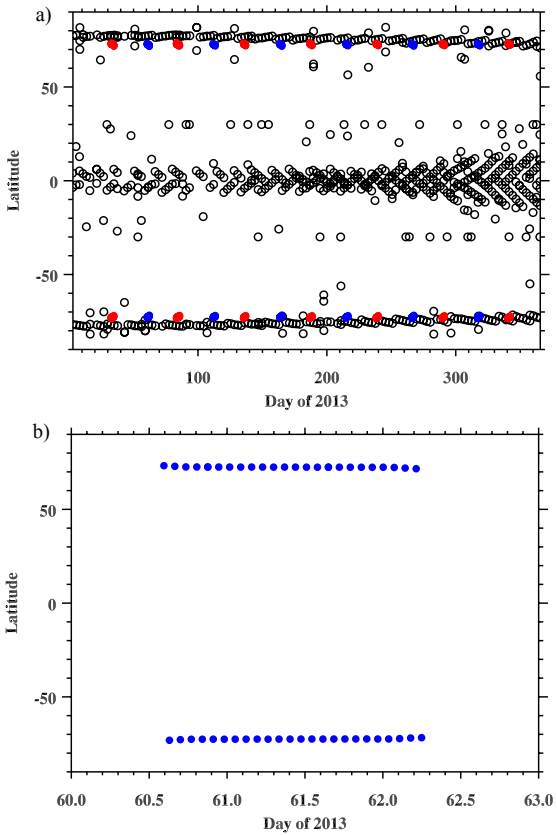

Figure 2. (a) Time Series of latitude distribution of SNO events of CrIS-ARIS (black), CrIS-IASI/A(red), and CrIS-IASI/B (blue), and **(b)** enlarged plot for the SNO event of CrIS-IASI/B on 1 March 2013.

AMTD
8, 7161–7199, 2015

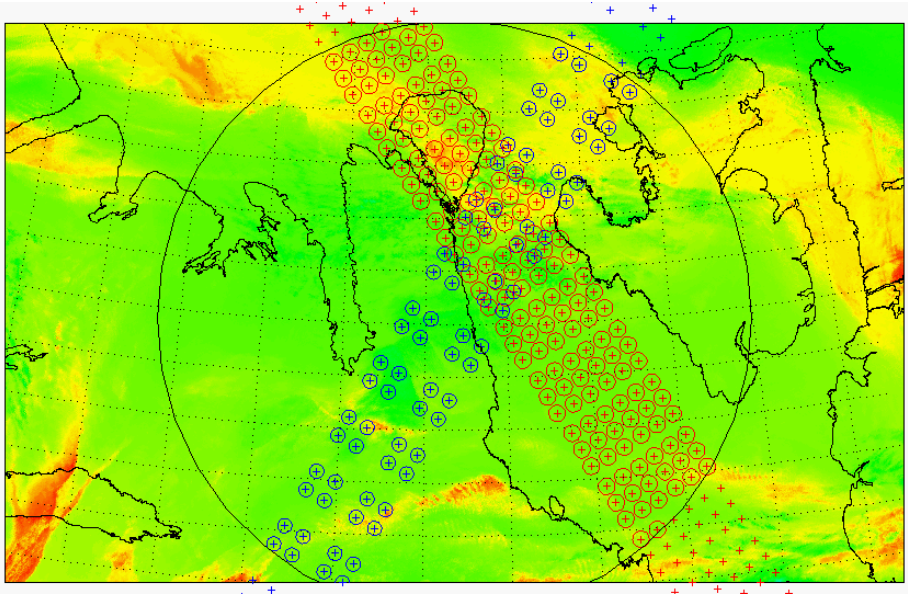

Figure 3. An example of a SNO event of SNPP and MetOp-A at 18:22:22 UTC on 27 August 2013. The blue circles indicate the IASI FOVs and the red ones denote CrIS FOVs at nadir view, where the VIIRS image at M16 band is superimposed.

AMTD
8, 7161–7199, 2015

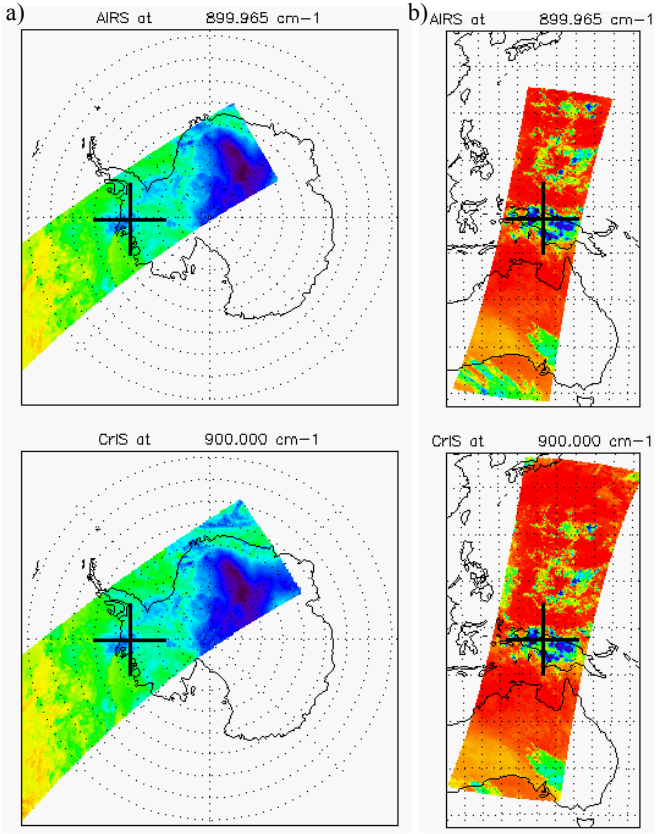

Figure 4. AIRS (top) and CrIS (bottom) images at 900.0 cm^{-1} for the Polar (left) and Tropical SNO (right) case, which occurred at 21:49 UTC and 16:15 UTC on 30 August 2013, respectively.

AMTD
8, 7161–7199, 2015

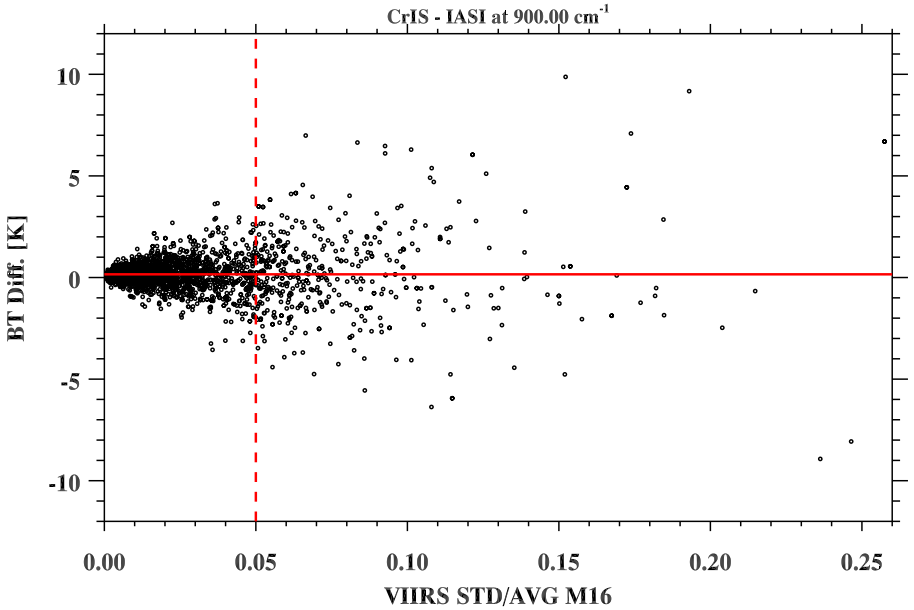

Figure 5. BT difference at 900 cm^{-1} between CrIS and IASI/B vs. the standard deviation to mean ratio of the VIIRS radiances in band M16. The horizontal line indicates the mean of CrIS-IASI BT differences with a value of 0.158 K and the standard deviation of BT differences is 1.34 K

AMTD
8, 7161–7199, 2015

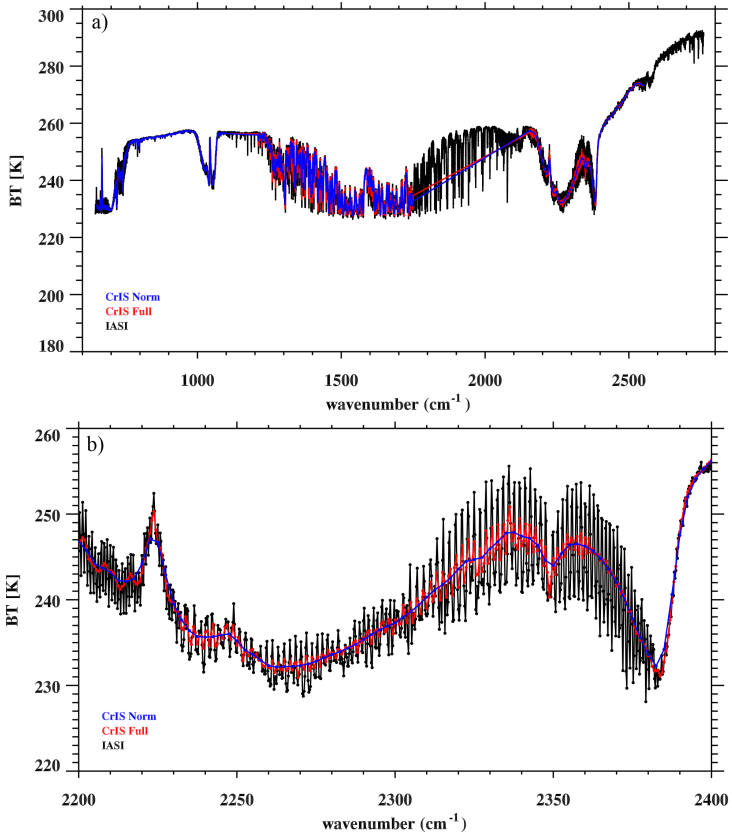

Figure 6. (a) CrIS and IASI Spectra for paired CrIS and IASI SNO FOVs on 27 August 2013 and **(b)** enlarged plot at the spectral range from 2200–2400 cm^{-1}.

AMTD
8, 7161–7199, 2015

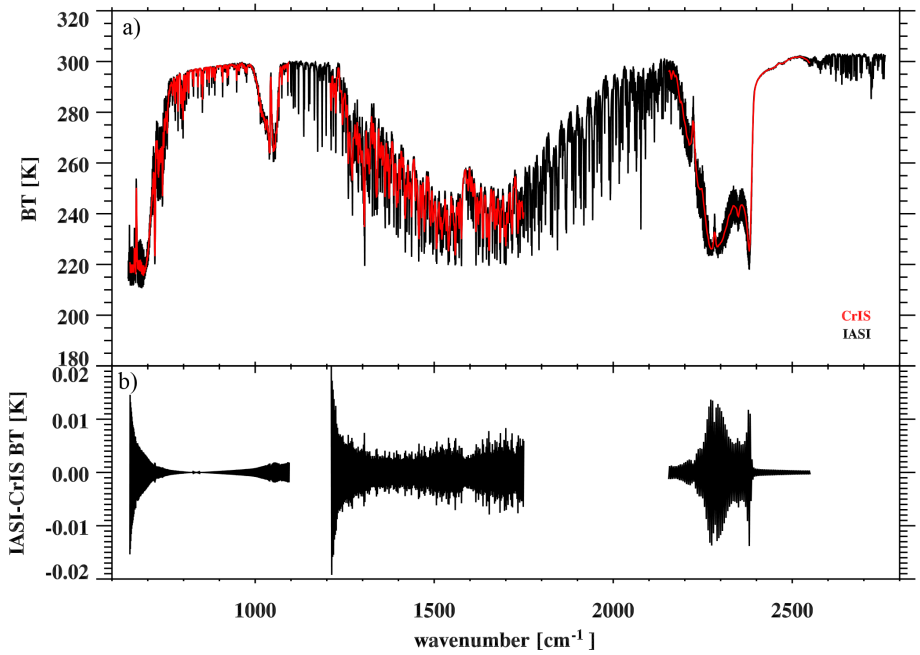

Figure 7. (a) CrIS (red color) and IASI (black) spectra simulated by LBLRTM using an identical atmospheric profile as an input and **(b)** their spectral differences. CrIS and IASI spectra are shown in their own spectral sampling resolution after apodization. Their BT differences are computed at the CrIS spectral grids by converting the IASI spectrum onto the CrIS spectral grids.

AMTD
8, 7161–7199, 2015

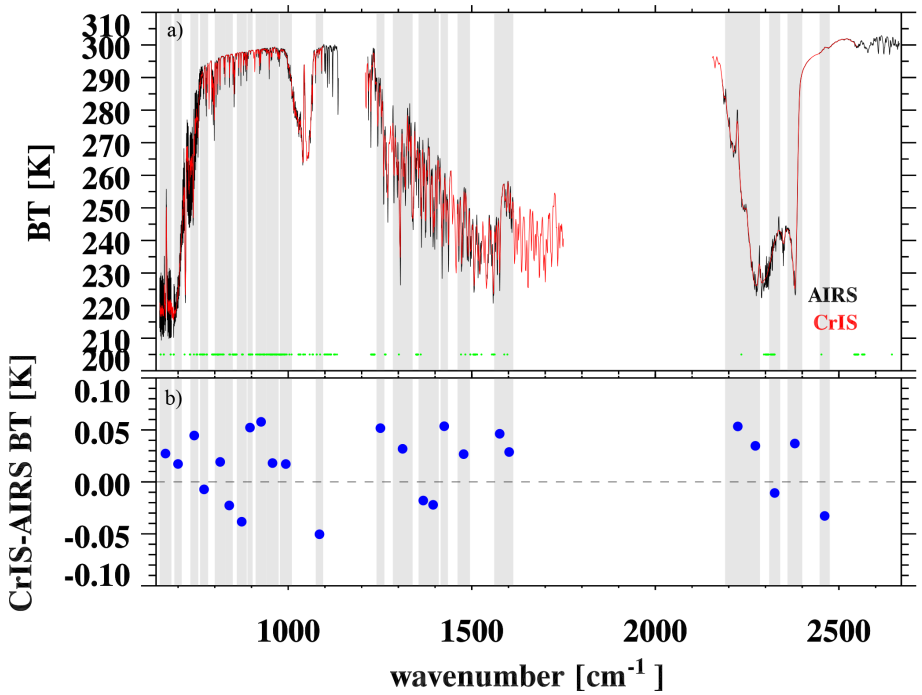

Figure 8. (a) CrIS (black) and AIRS (red) spectra simulated byLBLRTM using an identical atmospheric profile and **(b)** their spectral differences along the 25 spectral regions indicated by the gray bars. The green dots indicate the AIRS degraded or dead channels.

AMTD
8, 7161–7199, 2015

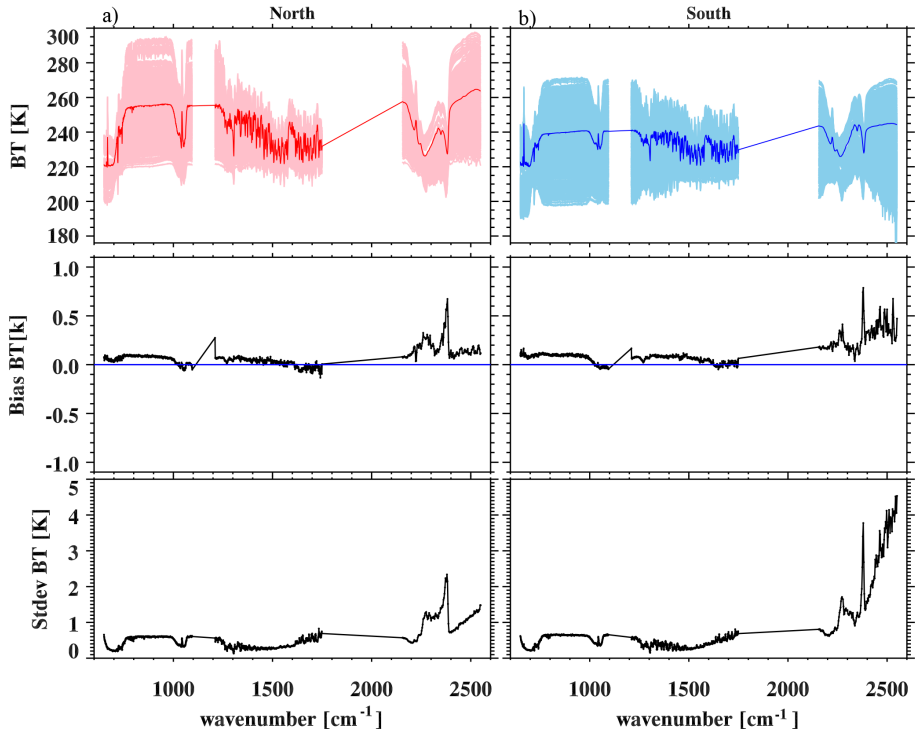

Figure 9. CrIS spectral distribution (top) for CrIS-IASI/A **(a)** North SNOs (left) and **(b)** South SNOs (right) and the mean (middle) and standard deviation (bottom) of CrIS-IASI/A BT differences. The solid lines in the top figure represent the average spectrum from all the samples.

AMTD
8, 7161–7199, 2015

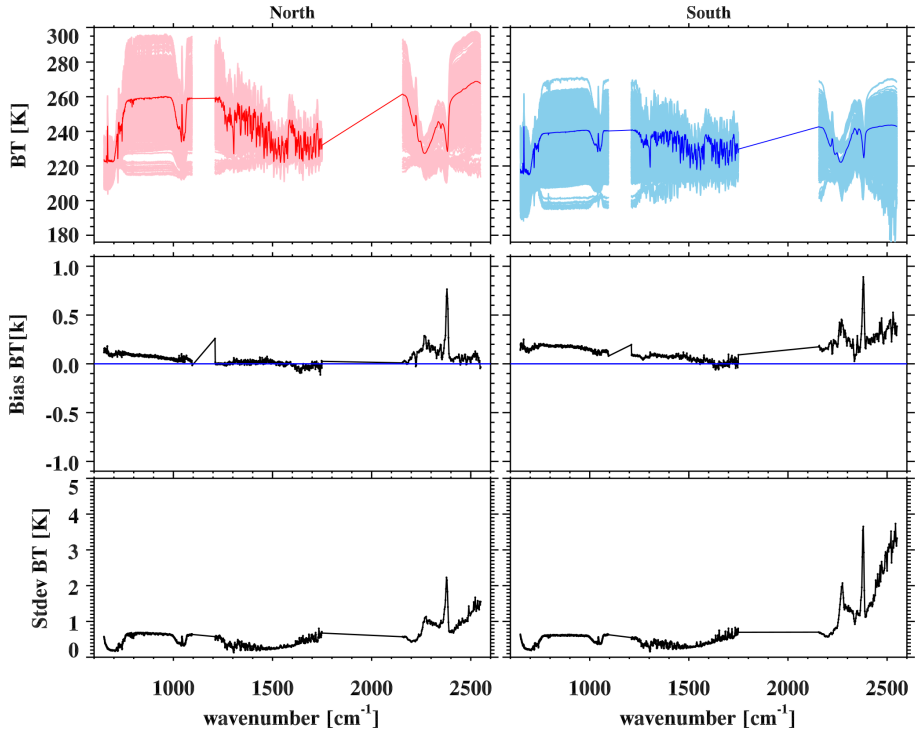

Figure 10. Same as Fig. 9 but for CrIS-IASI/B.

AMTD
8, 7161–7199, 2015

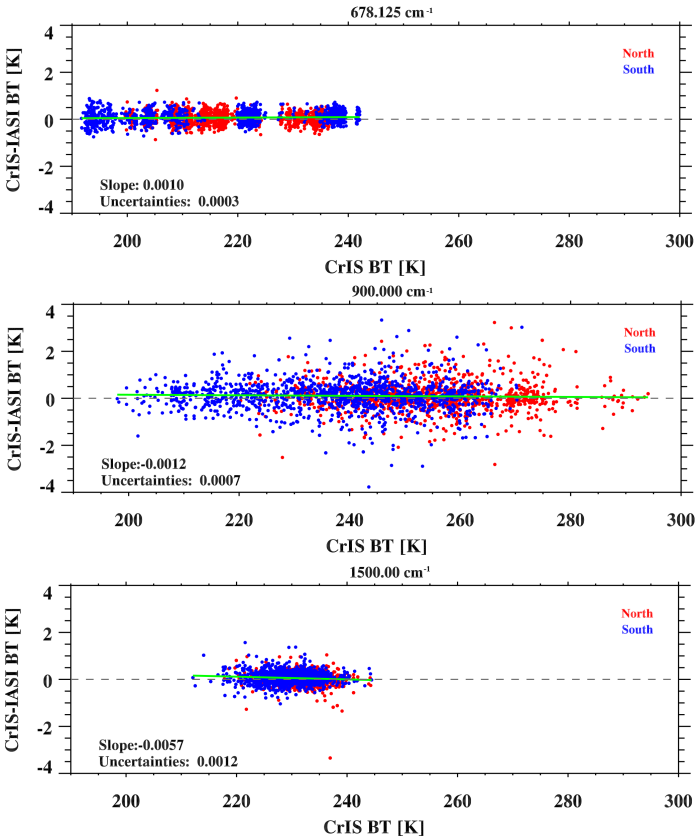

Figure 11. Scatter plots of CrIS-IASI/A BT differences vs. CrIS BT at 678.125, 900.0, and 1500 cm^{-1}. The red and blue dots represent the data from North and South SNOs and the green line is the linear regression line. The slopes and their one-sigma uncertainties are also listed.

AMTD
8, 7161–7199, 2015

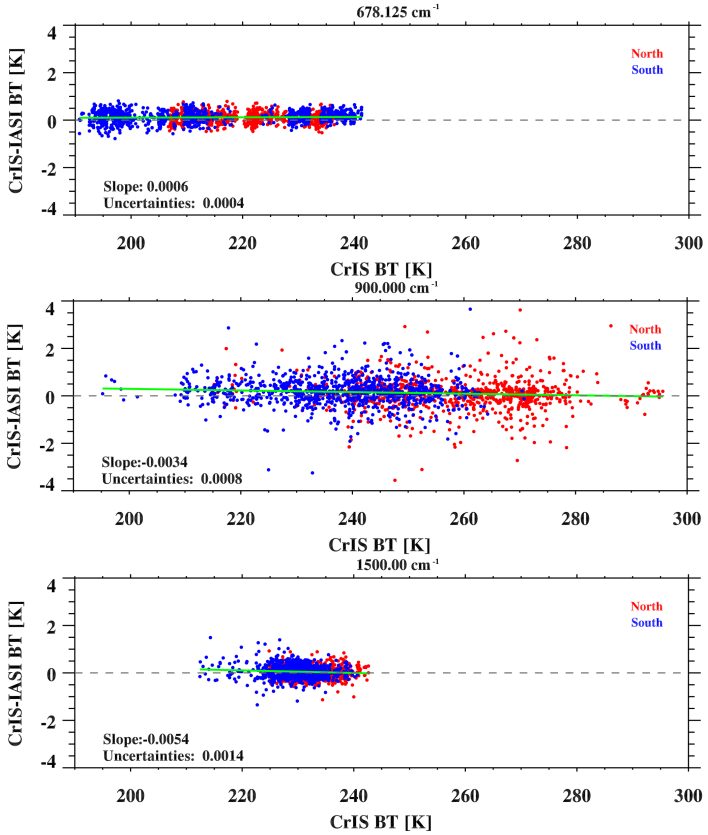

Figure 12. Same as Fig. 11 but for CrIS-IASI/B.

AMTD
8, 7161–7199, 2015

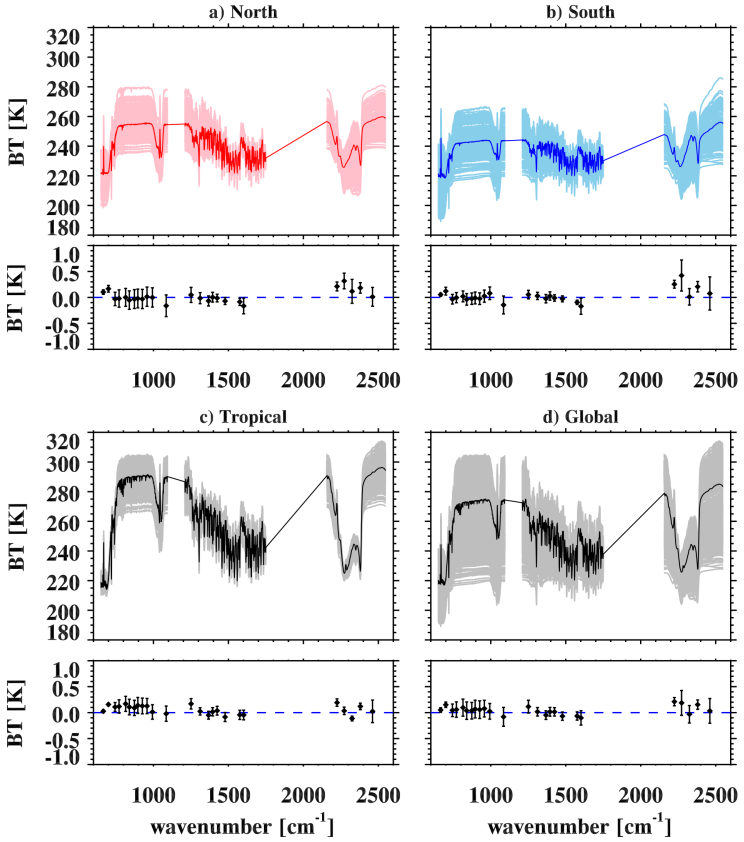

Figure 13. CrIS spectral distribution for CrIS-AIRS SNOs and their mean BT differences with the standard deviation along the 25 spectral regions, including **(a)** North SNOs, **(b)** South SNOs, **(c)** Tropical SNOs, and **(d)** the global dataset that combines three datasets together. The solid lines represent the average spectrum from the samples.

AMTD
8, 7161–7199, 2015

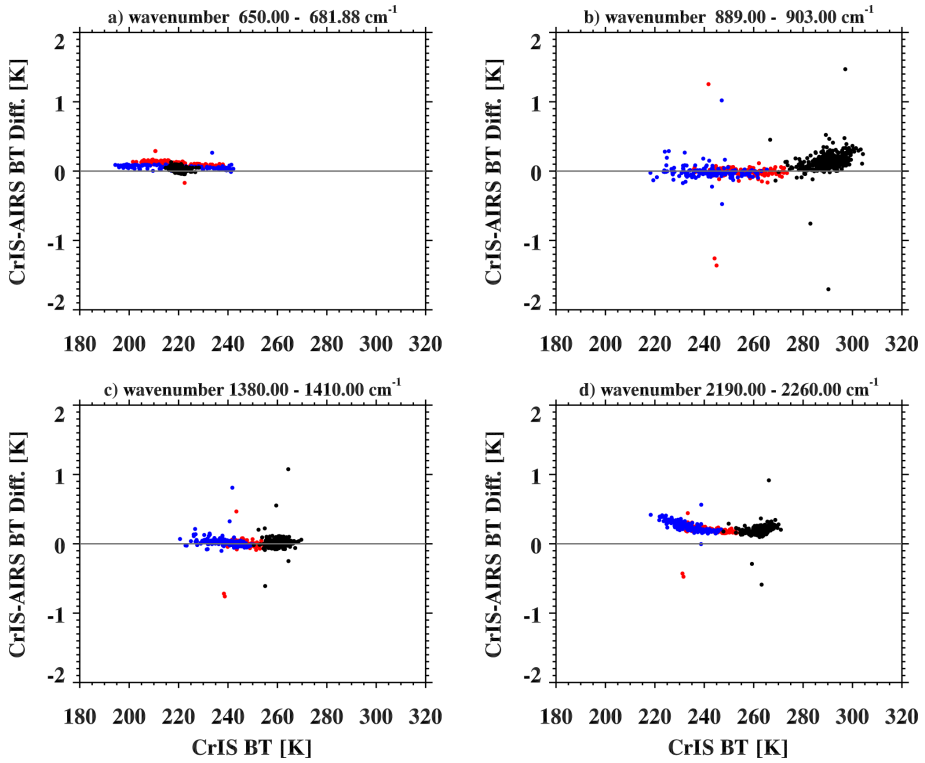

Figure 14. Scatter plots of CrIS-AIRS BT differences vs. CrIS BT at four spectral regions, **(a)** 650–681.88 cm^{-1}, **(b)** 889–903 cm^{-1}, **(c)** 1380.0–1410.00 cm^{-1}, and **(d)** 2190–2260 cm^{-1}. The red, blue, and black dots indicate the BT differences from North SNOs, South SNOs, and Tropical SNOs.

AMTD
8, 7161–7199, 2015

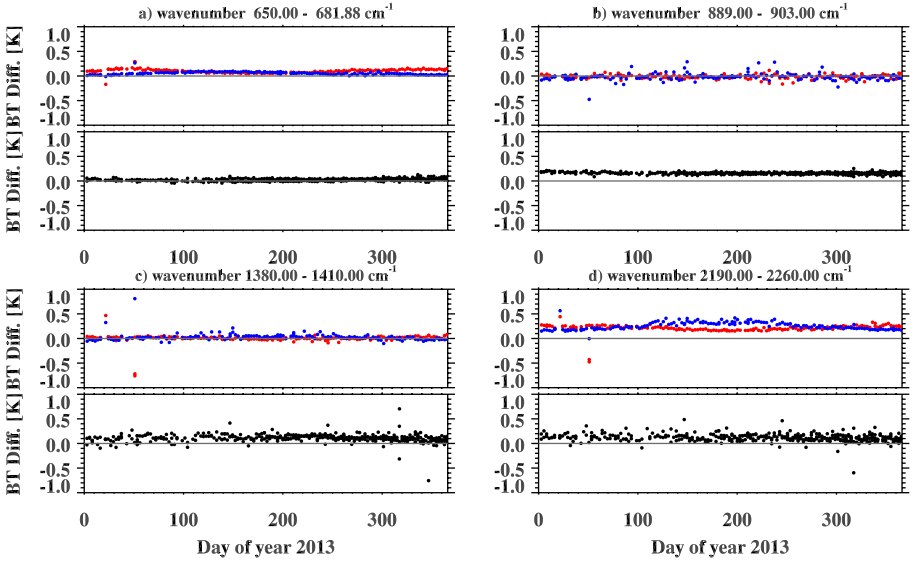

Figure 15. Time Series of CrIS-AIRS BT differences at four spectral regions, **(a)** 650–681.88 cm^{-1}, **(b)** 889–903 cm^{-1}, **(c)** 1380.0–1410.00 cm^{-1}, and **(d)** 2190–2260 cm^{-1}. The red, blue, and black dots indicate the BT differences from North SNOs, South SNOs, and Tropical SNOs.

AMTD
8, 7161–7199, 2015